Journal of Power Sources 690 (2026) 240825

Contents lists available at ScienceDirect

Journal of Power Sources

journal homepage: www.elsevier.com/locate/jpowsour

Modeling of internal short circuit-induced thermal runaway in anode-free lithium cells

Nitesh Gupta [a], Kaiqiang Qin [a], Tatsuro Sasaki [b], Koichiro Aotani [b], Chao-Yang Wang [a,*]

[a] *Electrochemical Engine Center (ECEC) and Department of Mechanical Engineering, The Pennsylvania State University, University Park, PA, 16802, USA*
[b] *Nissan Research Center, Nissan Motor Co. Ltd., Natsushima, Yokosuka, Kanagawa, 237-8523, Japan*

HIGHLIGHTS

- Electrochemical–thermal model for Internal short circuit-induced thermal runaway.
- Resistance-controlled Internal Short Circuit (RISC) inspired simulation framework.
- Joule heating triggers runaway, while oxygen-driven reactions dominate severity.
- Oxygen diffusion-controlled reactions govern thermal runaway onset and propagation.
- Model enables predictive safety screening for high-energy anode-free cells.

GRAPHICAL ABSTRACT

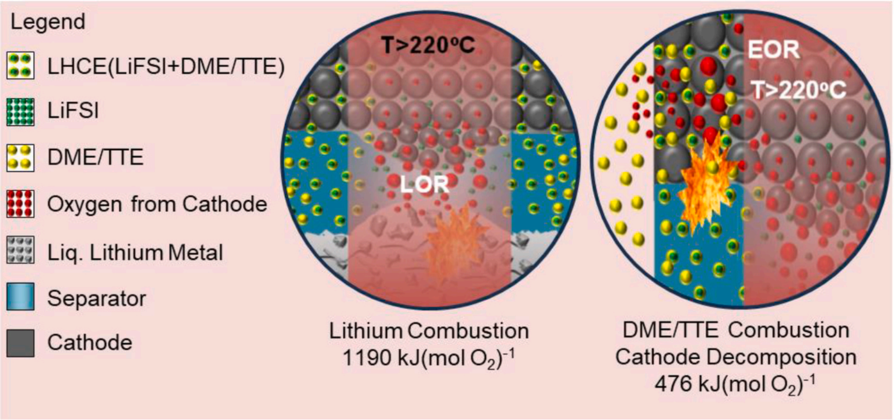

ARTICLE INFO

Keywords:
Anode-free cells
Internal short circuit
Thermal runaway
Oxygen diffusion
Safety
Abuse

ABSTRACT

Anode-free lithium batteries (AFBs) offer ultra-high energy density, but further work is needed to understand and manage issues associated with internal short circuits (ISCs) and thermal runaway (TR). In this study, an electrochemical-thermal coupled model is developed to simulate ISC-induced TR in anode-free cells. The model is inspired by the resistance-controlled internal short circuit (RISC) technique and is rigorously validated against experimental measurements. Localized Joule heating from the ISC is shown to act as the trigger for TR, while oxygen release from cathode decomposition and subsequent lithium oxidation and electrolyte oxidation reactions dominate the runaway energetics. A theory-based reaction framework coupled with oxygen diffusion captures the onset, propagation, and severity of TR with high fidelity. It is found that ISC heat primarily initiates runaway, whereas side reaction-driven heat governs propagation and intensity. This validated modeling provides quantitative insight into ISC-induced failure mechanisms and a modeling framework to support comparative safety assessment and design screening of high-energy anode-free batteries.

---

* Corresponding author.
E-mail address: cxw31@psu.edu (C.-Y. Wang).

https://doi.org/10.1016/j.jpowsour.2026.240825
Received 21 March 2026; Received in revised form 9 June 2026; Accepted 23 June 2026

1. Introduction

Emerging demands for energy-dense battery technologies in automotive and aircraft applications have driven intensive research on lithium-metal anodes and anode-free cell chemistry [1], [2], [3]. Lithium-ion batteries (LiBs) have an energy density of 100-265 Wh kg^{-1} [4], [5] and replacing them with anode-free batteries (AFBs) results in a 30% weight reduction and a >300 Wh kg^{-1} energy density [6]. AFBs can not only meet the energy density requirements of aircraft applications, but also fulfill the ideal automotive lifetime standard [7]. Moreover, anode-free concepts eliminate the slurry-coating, drying, and calendaring steps for the negative electrode, thereby simplifying the cell process flow and maintaining the existing LiB supply chain [8]. Salvatierra et al.'s [8] review indicates that ~75% of the manufacturing cost is attributed to materials, and removing the anode material reduces the cost by ~13%.

Despite these advantages, the applicability of AFBs remains questionable because abuse test studies have shown that AFBs/LMBs may ignite and produce fire and smoke under ISC conditions, sometimes within seconds [9]. They have a tendency to form lithium dendrites [10], experience high cycling stresses due to a ~20% volume change [3], and contain flammable compounds, creating a combination of factors that can increase fire risk under abuse [11]. Accidents involving LiB fires, such as EV battery fires [12], portable device fires [13], and data center fires [14], draw widespread attention and raise questions about the technology's legitimacy. Therefore, the safety of electric vehicles (EVs) and electric vertical take-off and landing (eVTOL) aircraft remains a barrier to their widespread acceptance [15], [16], [17], [18]. In this race to achieve the target lifetimes and energy densities, research focused on safety needs to advance correspondingly.

There are multiple types of abuse cases involving batteries, including mechanical [19] (crush, penetration), electrical (overcharge, overdischarge), and thermal (high/low temperature) [20], [21], [22], [23]. In many abuse cases, the separator is compromised, and an internal short circuit (ISC) occurs inside the cell. During an internal short, a large current flows through the small shorted area, leading to an instantaneous rise in local temperature ($dT/dt > 10000\,^{\circ}C\ min^{-1}$) [24], [25]. The question of whether this localized high temperature converts to thermal runaway (TR) and leads to cell or battery failure is uncertain and difficult to replicate experimentally. For example, Song et al. [26] reported different responses despite testing six identical cells using nail penetration, with results ranging from safe behavior to catastrophic combustion. The present methods aim to evaluate the safety of large-format batteries, but their inherent variability poses significant challenges to experimental reproducibility and systematic analysis. In the existing literature, abuse tests commonly used to assess battery safety such as ball crush [27], nail penetration [28], [29], [30], [31], embedding of low-melting-point materials [30], patch-heater triggering [32], and external short-circuit tests [33] typically lead to complete multi-layer shorting of the cell and often fail to provide quantitative,

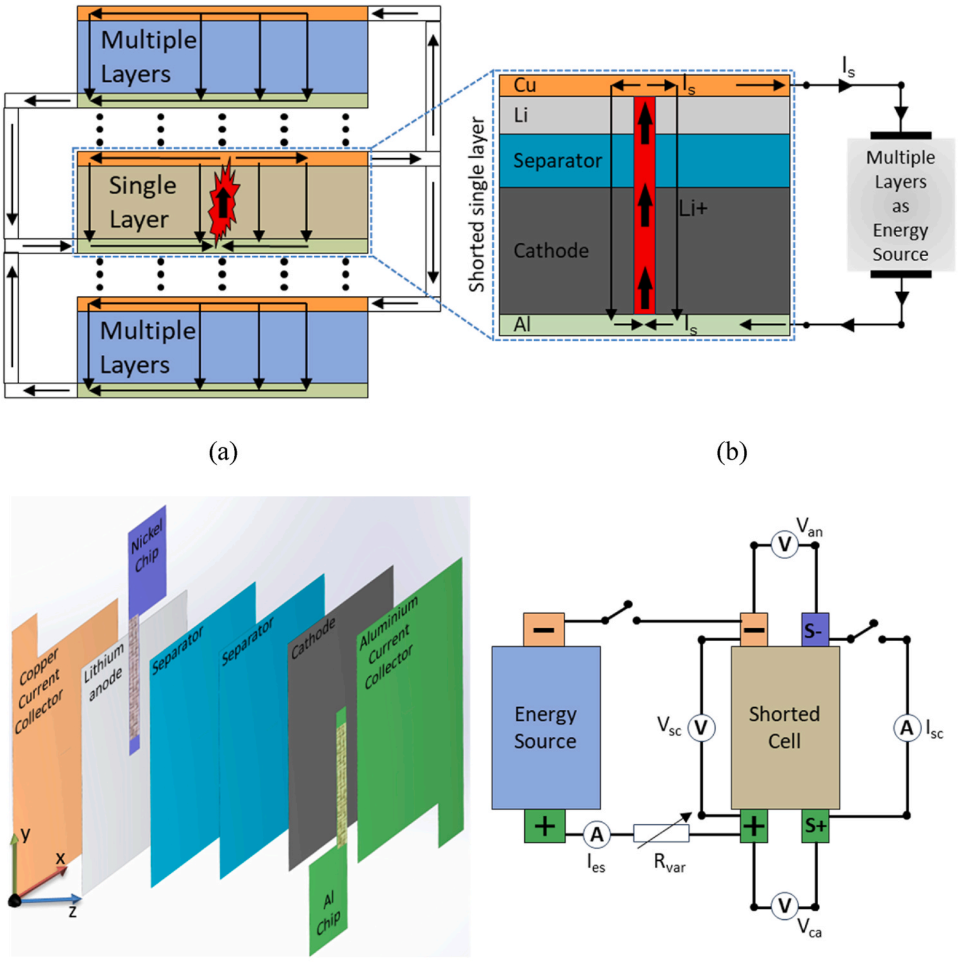

(a) (b)

(c) (d)

Fig. 1. Schematics of (a) Physical problem of ISC, (b) Simulation equivalent of RISC, (c) Exploded view of experimental shorted single-layer cell in RISC, (d) Electrical circuit for RISC.

well-controlled, and repeatable results. Moreover, past simulation work focuses solely on the ISC phenomenon, providing limited insights into improving battery safety [27], [34], [35], [36].

Given the current situation, there is a need to develop a simulation model for ISC-induced TR that can be validated with experimental data and serve as a baseline for analyzing the safety of an anode-free lithium cell. This study presents an electrochemical thermal-coupled (ECT) ISC-induced TR simulation model inspired by the resistance-controlled internal short circuit (RISC) technique [11], [24], [37]. The simulation model will be validated against experimental data from the RISC technique, and the validated model will provide deeper insights into thermal runaway.

2. ECT model

Fig. 1a shows the physical problem of ISC in which a single layer of a multi-layer cell is shorted at one location. In this simulation model, this single-layer shorted cell, representing the chemistry of interest, is examined while maintaining the dynamics of a high-capacity cell. Fig. 1b shows a schematic of the simulation problem. The shorted single-layer of the cell, which is of utmost interest, is thermally isolated [25] from other un-shorted layers and visualized/modeled separately. The shorted single-layer cell is connected in parallel with an energy source (ES), which represents unshorted layers that are less interesting during an ISC and only serve to supply current to the shorted cell. Dividing shorted and unshorted layers into two separate cells in parallel inherently consumes less computational power, as it allows us to use a fine mesh for the single-layer shorted cell and a coarse mesh for the unshorted multilayer cell. Conventional 3D multi-scale multi-domain models for multi-layer cells require the same mesh across all layers, resulting in a significantly larger number of elements and, consequently, greater computational expense. Moreover, the shorted single-layer cell can be thermally isolated from the unshorted layers, enabling focused analysis of the localized internal short-circuit (ISC) behavior while maintaining electrical coupling with the rest of the cell. This approximation can be justified by a thermal-diffusion scale analysis. The characteristic thermal diffusion length given by $\delta \sim \sqrt{\alpha t}$ $\sim$0.27 mm over a $\sim$3 s timescale (typical of ISC-triggered thermal runaway) is significantly smaller than the total thickness of a multilayer cell ($\sim$10 mm).

2.1. RISC experimental method

The RISC method has been described at length previously [11], [24], [25], [37]. The goal of using this technique in a simulation study is to use it as a tool for model validation. RISC visualizes the shorted single layer and unshorted multi-layers separately. Fig. 1c shows the exploded CAD view of the single-layer shorted cell used in the experiment. The cell has four terminals. The first terminal is for the copper (anode) current collector (CC), the second terminal is for the nickel chip, which is in direct contact with the copper CC inside the cell at the center (the rest of the chip is insulated). The third terminal is for the aluminum (cathode) CC, and the fourth terminal is for the aluminum chip, which is in direct contact with the aluminum CC inside the cell at the center (the rest of the chip is insulated). Fig. 1d shows the electrical connections of the experiment. The CC terminals are connected to the ES, and the nickel and aluminum chip terminals are connected to each other via a switch. A thermocouple is placed inside the cell between the separators to measure the instantaneous temperature at the shorted area.

When the switch is closed, a short circuit occurs between the anode CC and the cathode CC. The ES supplies current to the shorted area. The instantaneous current is measured at multiple locations by measuring the voltage drop over shunt resistors. One shunt is placed in series with chip terminals to measure total shorting current (I_{SC}), and another shunt is placed in series with the ES to measure the current supplied by the ES (I_{ES}). Fig. S1 shows the current path inside the single-layer cell. The current path is essential for understanding how to model accurate shorting resistance and hot spots within the cell. During an ISC, the current from the ES enters the cathode CC and flows into the Al chip. Through the chip, it exits the cell and flows into the wire connecting it to the Ni chip, where it re-enters the cell. It then enters the anode CC and exits the cell, returning to the ES. Therefore, the total short-circuit resistance would be the resistance across the two terminals of the ES, following the path of the current. These resistances are measured with the help of shunt resistances placed on the cathode side and anode side of the shorted cell. More information on the measurement and experimentation can be found in Ge et al. [24]. Table S1 shows the cell specifications for the ES and the single-layer shorted cell used in this study.

2.2. Numerical simulation model

The ECT model used to develop the ISC-TR simulation has been developed over the years [38], [39], [40], [41]. For brevity, all details of the electrochemical model are provided in the Supporting Information. Details of the cell design for the electrochemical simulation model are presented in Table S2. A nickel-cobalt-manganese (NCM811) cathode is used for both cells. An anode-free cell is used for the single-layer cell, and a graphite anode cell is used for the energy source. A localized high concentration electrolyte (LHCE) consisting of LiFSI salt in dimethoxyethane (DME) solvent and 1,1,2,2-tetrafluoroethyl-2,2,3,3-tetrafluoropropylether (TTE) diluent (1:1.2:3 by molar) is used in the AFB cell, and 1M LiPF6 in EC/EMC (3:7), a commercial electrolyte, is used for the LiB energy source.

The electrochemical model is coupled to the energy equation via temperature. Equation (1), an Arrhenius equation, is used to calculate cell properties at different temperatures, and the energy equation is used to solve for temperature.

$$\Phi = \Phi_{ref}\ exp\left[\frac{E_{act,\Phi}}{R}\left(\frac{1}{T_{ref}} - \frac{1}{T}\right)\right] \qquad \text{Equation 1}$$

Where, Φ is the property to be calculated, $E_{act,\Phi}$ is the activation energy related to the property, and R is the universal gas constant. Equation (2) gives the full energy equation.

$$\frac{\partial(\rho C_p T)}{\partial t} = \nabla.k\nabla T + q_{cell} + q_{short} + q_{TR} \qquad \text{Equation 2}$$

Where the first term represents the energy storage term, the second term represents the energy diffusion term, and the rest of the terms represent energy generation inside the cell. q_{cell} is the heat from electrochemical reactions, and from potential gradients in the electrode and the electrolyte of the single-layer shorted cell, its full equation is given in supplementary information. q_{short} is the Joule heat generated in the current path during an ISC and is given by Equation (3). q_{TR} is the heat generated by thermal runaway reactions, which is explained in detail in further text.

$$q_{short} = \frac{I_{sc}^2 R_{sc}}{V} \qquad \text{Equation 3}$$

Where I_{sc} and R_{sc} are shorting current and shorting resistance, respectively. R_{sc} is a direct function of temperature, as all materials have a positive coefficient of resistance with respect to temperature, and was included in the simulation model, details of which are provided in Table S3.

$$q_{TR} = \sum_j \sum_k c_{k,j}^{p_{k,j}} A_j\ exp\left[\frac{E_{a,j}}{RT}\right] M_k H_j \qquad \text{Equation 4}$$

q_{TR} is given by Equation (4) [41], [42]. Where k represents the component/species, and j represents the reaction. c is the normalized concentration of the species, A (s^{-1}) is the frequency factor for the reaction.

E_a (J mol^{-1}) is the activation energy for the reaction, and p represents the order of the reaction j with respect to specie k. M_k (kg m^{-3}) is the volume-specific content of reacting species k in jelly roll, and H_j (kJ kg^{-1}) is the heat generation from the reaction j. The thermal runaway heat presented in Equation (4) is written for all sets of reactions during a TR, and the total TR heat is the sum of the heat of all the TR reactions.

The next step in establishing a TR model is to determine the different reactions and their associated heats of reaction for an anode-free lithium cell system. The current literature indicates that different reactions can be categorized into four groups: melting or evaporation reactions, decomposition reactions, binary or ternary reactions, and combustion reactions. From literature [11], [18], [24], [41–47], the reactions can be classified as.

- DME evaporation
- Separator melting
- Lithium melting
- NMC811 decomposition/oxygen evolution
- DME/TTE combustion
- TTE evaporation
- SEI decomposition
- Lithium reacting LiFSI + DME/TTE
- LiFSI decomposition
- Lithium combustion

During an ISC event, the reaction heat from each of the above reactions needs to be calculated using Equation (4) and used in the energy equation to assess its effect on temperature. Table 1 compares the heat release from these reactions with the heat released from ISC. The heat release data for the reactions are taken from various differential scanning calorimetry (DSC) literature or are calculated directly from first principles.

It is evident from Table 1 that the heat release from evaporation, melting, and SEI decomposition reaction is too low compared to the ISC heat. It will be insignificant to model these reactions as their effect during an ISC would be negligible. To model the remaining reactions, we need to fit Equation (4) to the DSC data and determine the kinetic parameters Ea, A, p, and H associated with them, as described by Puthusseri et al. [41] and Parmananda et al. [42]. As this method of modeling requires DSC data, it is herein referred to as the *data-based approach*. Table S4 presents the fitted kinetic parameters and the Arrhenius equation for modeling the DSC curves of the different reactions. Fig. 2a (left) compares simulated and experimental DSC plots generated using the *data-based approach*. The DSC data for the cathode-electrolyte reaction is taken from Hou et al. [44]. The DSC data of the anode-electrolyte reaction is taken from Guo et al. [45]. To model the heat release from lithium combustion, the TGA data of cathode decomposition was used [44]. The cathode decomposition equation in Table 1 shows all possible global reactions for oxygen release from the cathode, which results in a weight loss of 9-15.3%. The TGA data suggest that the weight loss is ~13% which matches exactly with the chemical reactions. The released oxygen is converted to heat via the lithium oxidation reaction (Table 1). For *data-based approach*, the assumption of oxygen reacting instantly with lithium was made, and a threshold of 290 °C based on findings from RISC was chosen, below which no TR was seen.

The *data-based approach* is a fast and reliable method widely used in the current literature, but it has drawbacks that can lead to incorrect results when simulating ISC-induced TR. The first disadvantage is the availability of accurate data; although DSC is a fundamental technique, the reactant ratios used in experiments can affect the results. Ideally, reactants should be used in the same ratio as in the final cell; however, since there are no established guidelines, researchers often use different ratios. The DSC data for AFB cells in the current literature lack independent species studies. As a result, using DSC data tends to overestimate heat generation. For instance, the DSC of cathode electrolyte reactions shown in Fig. 2 includes three fundamental reactions: cathode decomposition, LiFSI decomposition, and solvent combustion. Similarly, the DSC of anode electrolyte reactions involves the decomposition of LiFSI, the anode-LiFSI reaction, and solvent combustion. Clearly, overlapping reactions lead to an overestimation of heat generation and an underestimation of the species consumed. The second disadvantage is finding the correct kinetic parameters for a given set of DSC data. Parameters fitted from DSC data obtained at a single scanning rate (°C min^{-1}) may yield unreliable results at a different rate. Therefore, it is important to fit the kinetic parameters using DSC data from multiple experiments conducted at various heating or scanning rates. The third issue relates to the assumption of oxygen evolution and consumption, which leads to a lithium oxidation reaction (LOR) as soon as oxygen is released from the cathode. This assumption does not account for delays caused by oxygen diffusion and migration, as well as its consumption in other oxidation reactions. Given the modeling and data issues with the *data-based approach*, next, we introduce a more robust model grounded in fundamental principles.

The *theory-based approach* identifies each reaction individually and breaks them into more fundamental reactions. The cathode electrolyte reaction splits into cathode decomposition/oxygen evolution and solvent combustion, while the anode electrolyte reaction splits into LiFSI decomposition and the Li-LiFSI reaction. The lithium oxidation reaction (LOR) and the electrolyte oxidation reaction (EOR) are modeled as functions of oxygen diffusion from the cathode to the anode. Fig. 2b (right) shows the DSC plots of the Cathode decomposition and LiFSI decomposition, respectively. The total heat from these reactions is negligible for a cathode active material weight of 0.762g and LiFSI weight of 0.08654g. Hence, it will be justifiable not to model these TR reactions in the *theory-based approach.*

The anode-salt reaction is a critical step in TR, as it has been shown to produce high heat across different cell chemistries. For example, the studies [44], [45], [48] show that graphite reaction with LiFSI generates considerable heat release starting at 200 °C. In particular, for AFBs, the literature lacks data on the reactions of Li and LiFSI. Possibly, the

Table 1
Reaction heat comparison.

Reaction sets	Reaction equation	T_{onset} (^{o}C)	Heat release(J/cm^2)
Internal short circuit	Joule heat generation in a short element	25	~70[b] [24], [25]
DME, TTE evaporation	DME(l) + TTE(l) → DME(g) + TTE(g)	90	−1.64$^{\text{calculated},a}$
SEI decomposition	SEI decomposition → $Li_2CO_3 + Li_2O$	90	0.22 [18], [43]
Separator melting	PP/PE(s) $((C_2H_4/C_3H_6)_n)$ → PP/PE(l)	140	−0.22$^{\text{calculated},a}$
Li melting	Li(s) → Li(l)	180	−0.22$^{\text{calculated},a}$
Cathode decomposition	$Li_{0.24}Ni_{0.8}Co_{0.1}Mn_{0.1}O_2 \rightarrow 0.24LiM_2O_4 + 0.52MO + 0.26O_2$	220	66 [44], [45]
Oxygen evolution	$Li_{0.24}Ni_{0.8}Co_{0.1}Mn_{0.1}O_2 \rightarrow MO + 0.12Li_2O + 0.44O_2$	220	
Solvent combustion	$C_4H_{10}O_2 + 5.5O_2 \rightarrow 4CO_2 + 5H_2O$ $C_5H_4F_8O + 3.5O_2 \rightarrow 4HF + CF_4 + 4CO_2$	220	
Anode-electrolyte reaction	Li + LiFSI + DME,TTE → HF, SO_2, LiF, CF_3SO_2	200	15.3 [46], [47]
Salt decomposition		220	
Lithium combustion	$Li + 0.25O_2 \rightarrow 0.5Li_2O$	180	37.8 [11]

[a] The values are calculated based on the loading and area of the single-layer AFB cell presented in Table S1.

[b] calculated based on short element area.

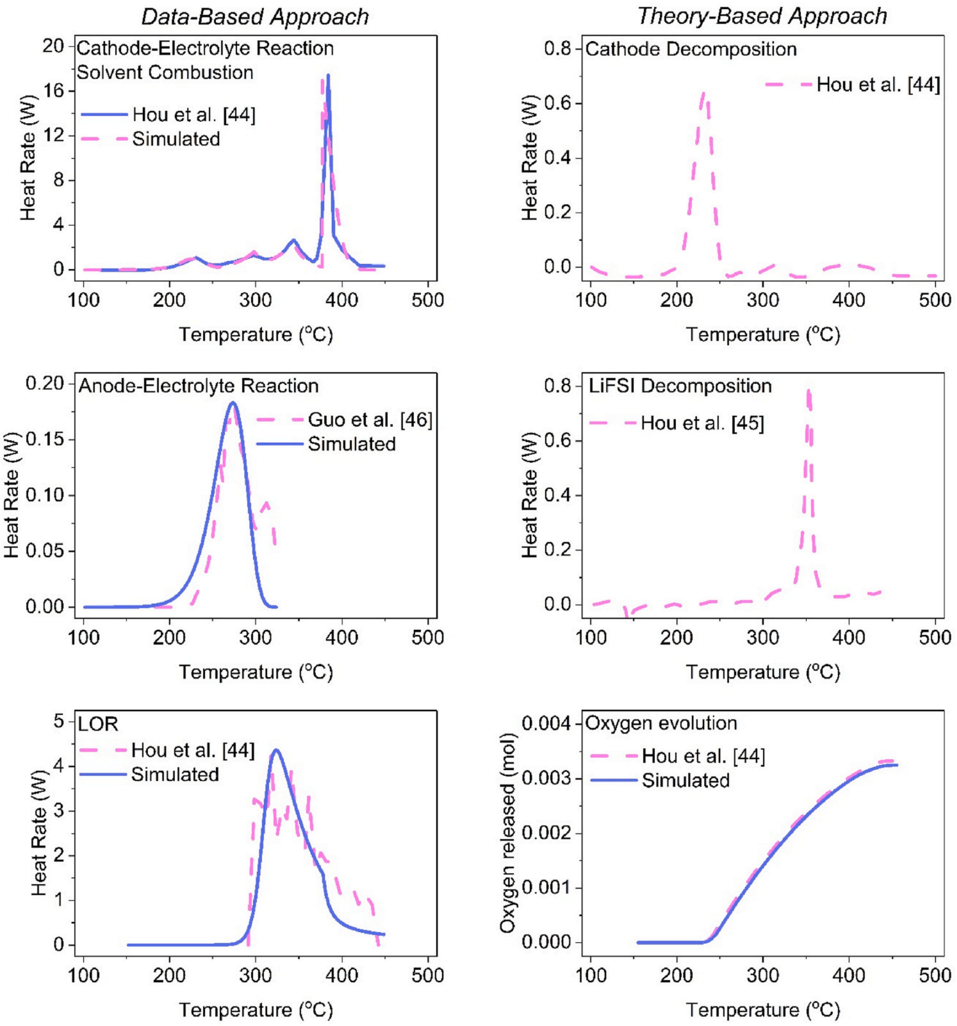

(a)

(b)

Fig. 2. Comparison of simulated and experimental DSC plots for (a) *data-based approach*. (b) *theory-based approach*.

reaction follows Equation (5), but there is a missing link as the equation cannot be balanced. Therefore, due to the unavailability of data on the formation heats and reaction coefficients, it is not presently possible to calculate the heat generated from this reaction. Moreover, Fig. S2 clearly shows that the reaction between Li and LiFSI is not a decisive factor for fires during ISC situations. It shows the RISC experiment for three different cases. The baseline case which is for the liquid AFB cell, case 2 is the liquid-free cell, and case 3 is the ionic liquid ($Py_{13}TFSI$; IL) cell. The liquid-free cell does not contain LiFSI salt, and the ionic liquid case contains a salt that does not react with lithium. Nevertheless, all three cells ignited under the tested conditions and exhibit similar timescales, indicating no decisive effect from the Li-LiFSI reaction. Therefore, due to the uncertainty in the effect of this reaction, it is better not to model this reaction in the theory-based model.

$$LiN(SO_2F)_2 + Li \rightarrow LiF + NO_2 + SO_2 \qquad \text{Equation 5}$$

To simulate the LOR and EOR, we now need to include the *oxygen diffusion model*. This governs the movement of oxygen from the cathode to the anode and its consumption in EOR and LOR in the separator and the anode, respectively. Oxygen diffusion is governed by Fick's law. Equation (6) and Fig. S3 show the 1D Fick's law.

$$\frac{\partial c_o}{\partial t} = D_{eff}\frac{\partial^2 c_o}{\partial x^2} \pm S \qquad \text{Equation 6}$$

$$S = -K_r\ c_o \qquad \text{Equation 7}$$

The source or sink term (S) is applied in two domains, the cathode and the separator. The cathode is modeled as a volumetric oxygen source, using TGA data (Fig. 2b) as the input. The separator is modeled as a volumetric sink, with the rate of the electrolyte oxidation reaction (EOR) defined in Equation (7) as the sink magnitude, where K_r is the reaction rate and c_o is the oxygen concentration in each domain. Another sink is modeled at the boundary between the separator and the anode to account for LOR, with the boundary concentration set to 0 mol. This means, above 180 °C, the rate of reaction of LOR is high enough to instantaneously consume all the oxygen diffused to the anode separator boundary.

In Equation (6), D_{eff} is the effective diffusivity of oxygen, defined for each domain and depends on the tortuosity and phase of each domain. Equation (8) defines D_{eff} numerically. It can be visualized that at higher temperatures, both liquid and gas phases will be present in each domain. The oxygen released from cathode decomposition will exist in both dissolved (in the liquid electrolyte) and gaseous phases due to rapid temperature rise, gas generation, and electrolyte evaporation. Under such conditions, oxygen transport may not be described by a single-phase diffusivity. Instead, it will be governed by combined transport through liquid-filled pores and gas-filled regions. So, D_{eff} will be the sum of the diffusivities of oxygen in the gas (D^{gas}) and liquid (D^{liq}) phases. The local distribution of gas and liquid phases is not directly measurable and varies due to electrolyte evaporation, gas generation, and structural changes within the porous media. Moreover, the order of magnitude difference between the diffusivity value of oxygen in gas and liquid is of *O(4)*. Therefore, it will be difficult to find the D_{eff} experimentally. Hence, this will serve as a fitting factor to match the temperature rise from the ISC-TR experiment data (RISC) and the ISC-TR simulation data.

$$D_{eff} = D^{liq}\varepsilon_{liq}^{\beta} + D^{gas}\varepsilon_{gas}^{\beta} \qquad \text{Equation 8}$$

For modeling the reaction rate *(K_r)*, two reactions are considered: the lithium oxidation reaction (LOR) and the electrolyte oxidation reaction (EOR), characterized by $K_{r,\ LOR}$ and $K_{r,\ EOR}$, respectively. The parameter $K_{r,\ EOR}$ governs the electrolyte oxidation reaction; increasing or decreasing it affects the rate at which EOR consumes oxygen and generates heat. A higher $K_{r,\ EOR}$ increases oxygen consumption in the separator, thereby reducing the amount of oxygen reaching the anode for LOR. However, because the model is transport-coupled, increasing $K_{r,\ EOR}$ does not shift the onset of thermal runaway, as this process is limited by oxygen diffusion to the reaction sites. While a higher $K_{r,\ EOR}$ increases the total oxygen consumed and heat generated by EOR, it does not significantly change the heat generation rate, which remains governed by mass transport limitations. A lower $K_{r,\ EOR}$ reduces both the rate and total oxygen consumed by EOR and delays the onset of thermal runaway, but only until LOR becomes dominant. Due to the lack of dedicated experimental data for EOR, $K_{r,\ EOR}$ is treated as a fitting parameter. With these inputs in Equations (6)–(8), Fick's law is solved using the initial and boundary conditions defined by Equations S12, S13, and S14.

The oxygen sink in the separator and the separator-anode boundary is converted to heat generated according to Equations 9 and 10, respectively. The heat of combustion in the two equations is calculated considering a complete combustion of the fuel. The fuel in LOR is lithium, and the fuel in EOR is a mixture of DME and TTE, which are hydrocarbon solvents. For a single-layer shorted cell, the amount of lithium is calculated based on the lithium deposited after charging.

$$\mathrm{Li} + 0.25\mathrm{O_2} \rightarrow 0.5\mathrm{Li_2O}\ \ \Delta H = 4.3 \times 10^7\ \mathrm{J\ kg^{-1}}\ \text{(reaction enthalpy, [11])} \qquad \text{Equation 9}$$

$$[0.714(\mathrm{C_5H_4F_8O}) + 0.286(\mathrm{C_4H_{10}O_2})] + 4.07\mathrm{O_2} \rightarrow 3.643\mathrm{CO_2} + 2.144\mathrm{H_2O} + 1.071\mathrm{CF_4} + 1.428\mathrm{HF}\,\Delta H = 1.13 \times 10^7\ \mathrm{J\ kg^{-1}}\ \text{(reaction enthalpy, [11])} \qquad \text{Equation 10}$$

3. Results and discussion

For all performance simulations, GT-Autolion 1D was employed, while for ISC-induced TR simulations, COMSOL v6.2 3D was utilized. The number of mesh elements for the single-layer shorted cell consists of 83,538 domain elements, 28,008 boundary elements, and 2835 edge elements. For the multi-layer energy source, these numbers are 18,200 domain elements, 6756 boundary elements, and 726 edge elements. Although the multi-layer cell has 20 layers, resulting in roughly five times fewer mesh elements than the single-layer cell, this configuration allows us to accurately capture high gradients near the shorting area. Fig. S4 shows a screenshot of the mesh for the single-layer cell, directly taken from a COMSOL model.

3.1. Validation

Specific steps for modeling and validating the ISC-induced TR model are shown in Fig. S5. It starts with designing the virtual cell and tweaking its electrochemical properties to match its performance characteristics with actual cell data. After that, the short element is modeled, and the cell is simulated for ISC. The shorting resistances and thermal properties of the cell are tweaked to match the ISC characteristics of the actual cell. Using this model, Gupta et al. performed parametric simulations for ISC in anode-free cells [25]. The next step involves coupling the ISC model with the TR model using temperature and species conservation. Finally, ISC-induced TR is simulated, and the kinetic triplets (data-based approach) or oxygen diffusivity (*Theory-based approach*) are fitted to match the temperature and time scale of thermal runaway with the actual cell data.

To validate the electrochemical properties, the performance curves for a single-layer shorted cell and a multi-layer energy source were compared and matched. A multiplication factor was calculated for each cell property so that the error between experimental and numerical discharge data is less. Table S5 presents the fitted electrochemical properties of the cells, while Fig. S6 displays the calibrated performance curves. Both figures show good agreement between experiment and simulation data.

To validate the ISC-induced TR model, the simulation results were compared with the RISC experiment results. The temperature and the TR time were matched between experiment and simulation by adjusting D_{eff}^{ca}, D_{eff}^{sep} and K_r. After fitting a D_{eff}^{ca} value of 1.2e-9 $\mathrm{m^2\ s^{-1}}$, D_{eff}^{sep} value of 2.1e-9 $\mathrm{m^2\ s^{-1}}$ and a K_r value of 55 $\mathrm{s^{-1}}$ was chosen. The fitted values for effective diffusivities (10^{-9} $\mathrm{m^2s^{-1}}$ range) are physically reasonable and lie between typical liquid- and gas-phase limits, consistent with a mixed-phase transport regime. Fig. 3a shows the terminal voltage (V), internal short-circuit current (I_{SC}), shorting chip temperature, and total short-circuit resistance (R_{SC}) results from the fitted simulation model compared with experimental results. When the single-layer cell is shorted, the system's (single-layer + energy source) terminal voltage drops instantaneously, and a current surge is observed. The joule heat ($I_{SC}^2R_{SC}$) from the current results in a large heating rate (dT/dt) and large temperature gradients. As the temperature increased, the materials' internal resistance increased, resulting in a rise in the total short-circuit resistance. This increase in resistance reduces short-circuit current. The combined effects of increased ion transport, chemical kinetics, and resistance due to increased temperature result in a recovery of voltage. Exact matching of the temperature data was challenging due to differences in construction, insulation, and environmental conditions between the physical tests and simulations, which were deemed insignificant to replicate in the modeling. As the electrochemical and energy equations show, cell properties depend strongly on temperature, and a slight difference in temperature profiles will result in corresponding differences in all results. Therefore, there is a slight difference between the V and I_{SC} modeling and the experimental results. The simulation model shows good agreement with the problem's physics and predicts the correct ISC and TR parameters. It also correctly predicts the TR time, indicating accurate prediction of local heat generation and underlying TR reactions.

Fig. 3b shows the TR parameters for the LHCE-based AFB. It gives more insights into the cell during a TR event. Before the maximum anode temperature reaches 220 °C, heating is solely due to joule heating from ISC. Once some area of the cell reaches 220 °C, oxygen begins to evolve and diffuse, reacting with the electrolyte and lithium. The first row of the plot shows the O_2 release and consumption rates, as well as the total oxygen released and consumed. O_2 is released at the cathode, diffuses to the separator, where it is consumed by EOR, and the remaining O_2 then diffuses to the anode, where it is consumed by LOR. There is no oxygen release until ~1.6s because the maximum cathode temperature before then is below 220 °C, which indicates the onset of cathode decomposition and O_2 release. The delay between the start of oxygen release and its consumption in the separator and anode is due to diffusion, which can be explained by calculating the mass diffusion time, $t \sim \frac{\delta^2}{2D}$. Using this equation, a diffusion time of 0.15s to 0.45s is expected, which is reflected from simulation results. The second row of this figure shows the heat generation from TR reactions (LOR + EOR) and ISC Joule

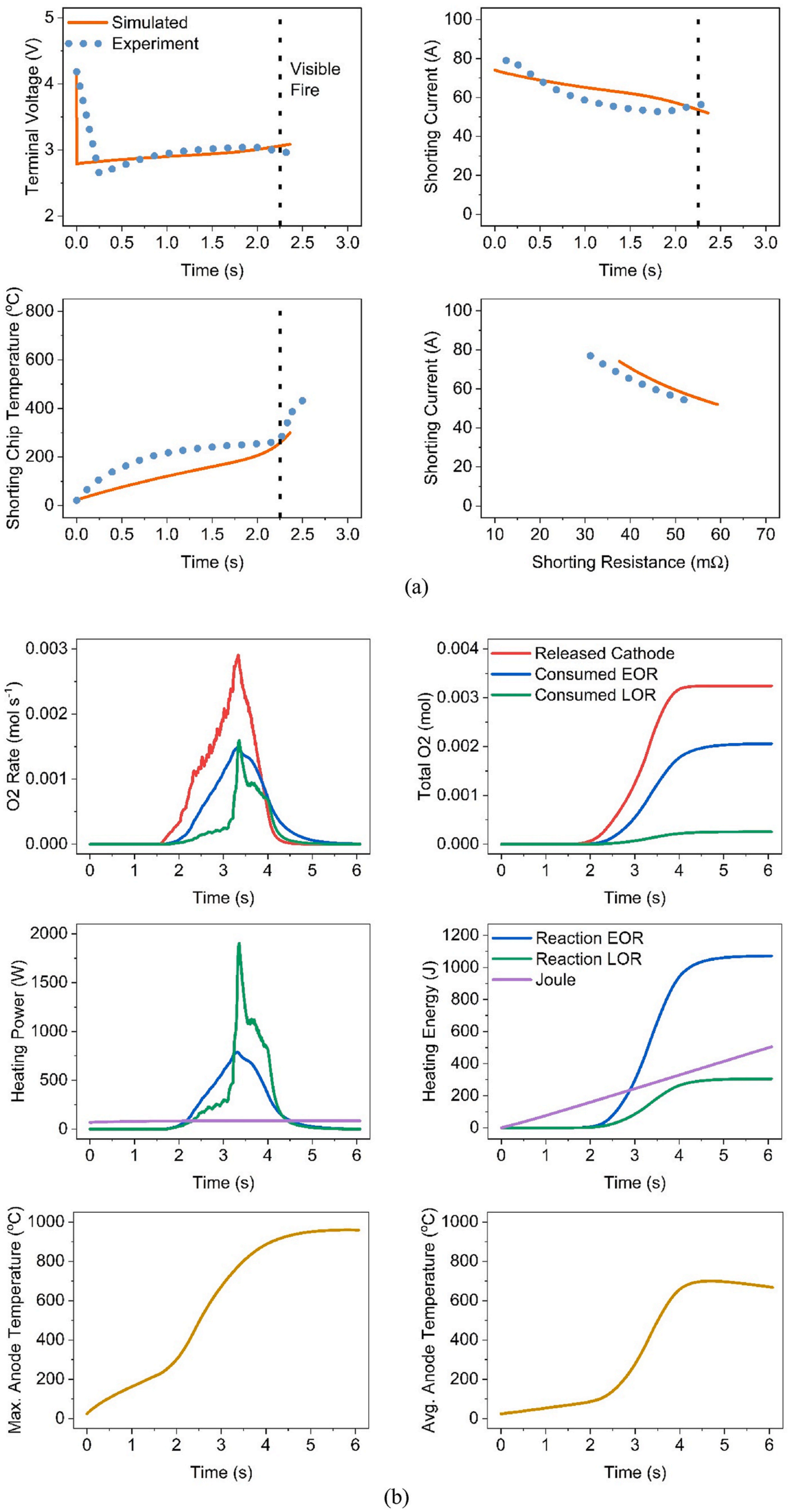

Fig. 3. Results for (a) Experiment and simulation comparison of ISC-induced TR. (b) TR parameters.

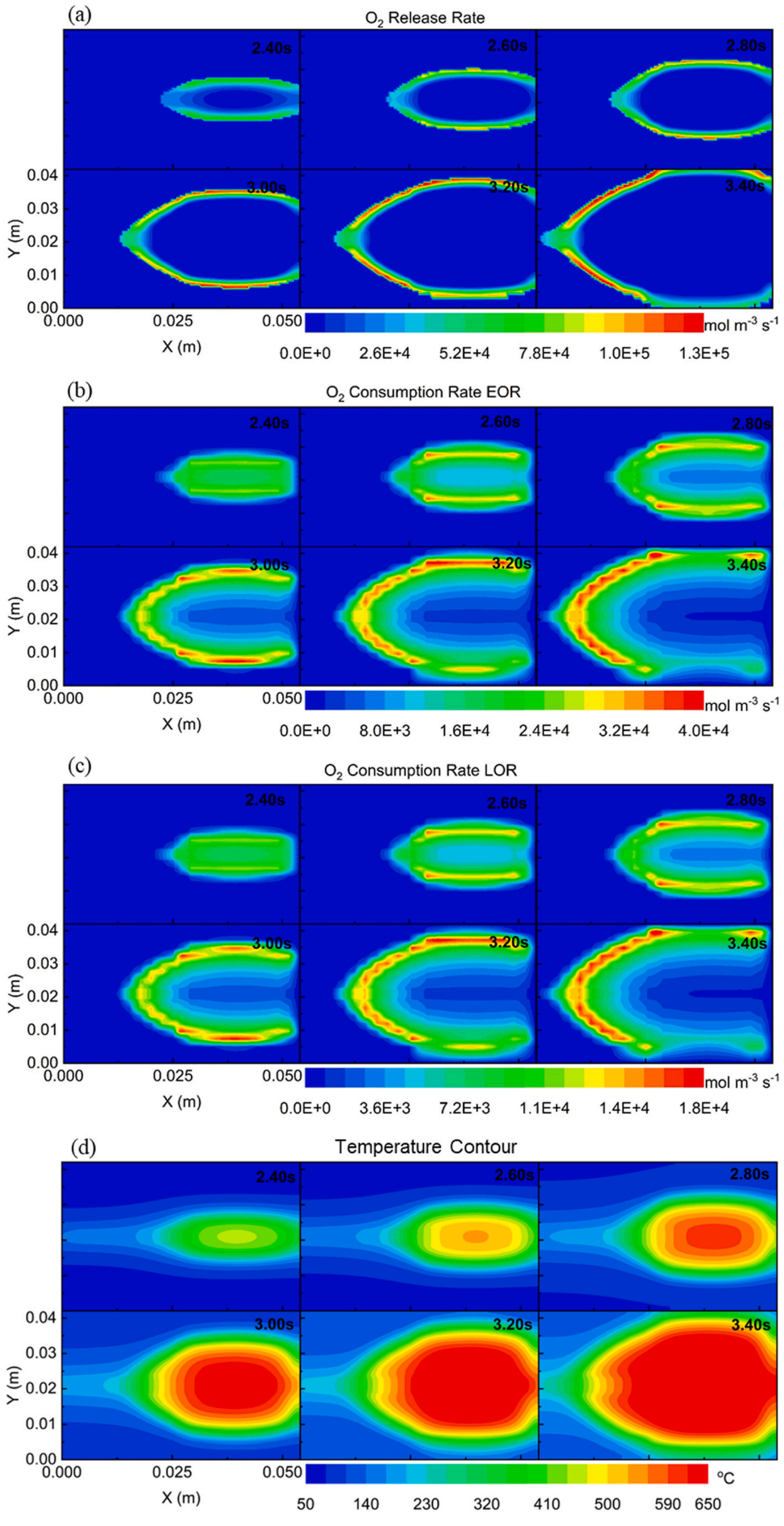

Fig. 4. Surface contours at different times near the TR propagation time, (a) O_2 release rate, (b) O_2 consumption rate by EOR, (c) O_2 consumption rate by LOR, (d) Temperature.

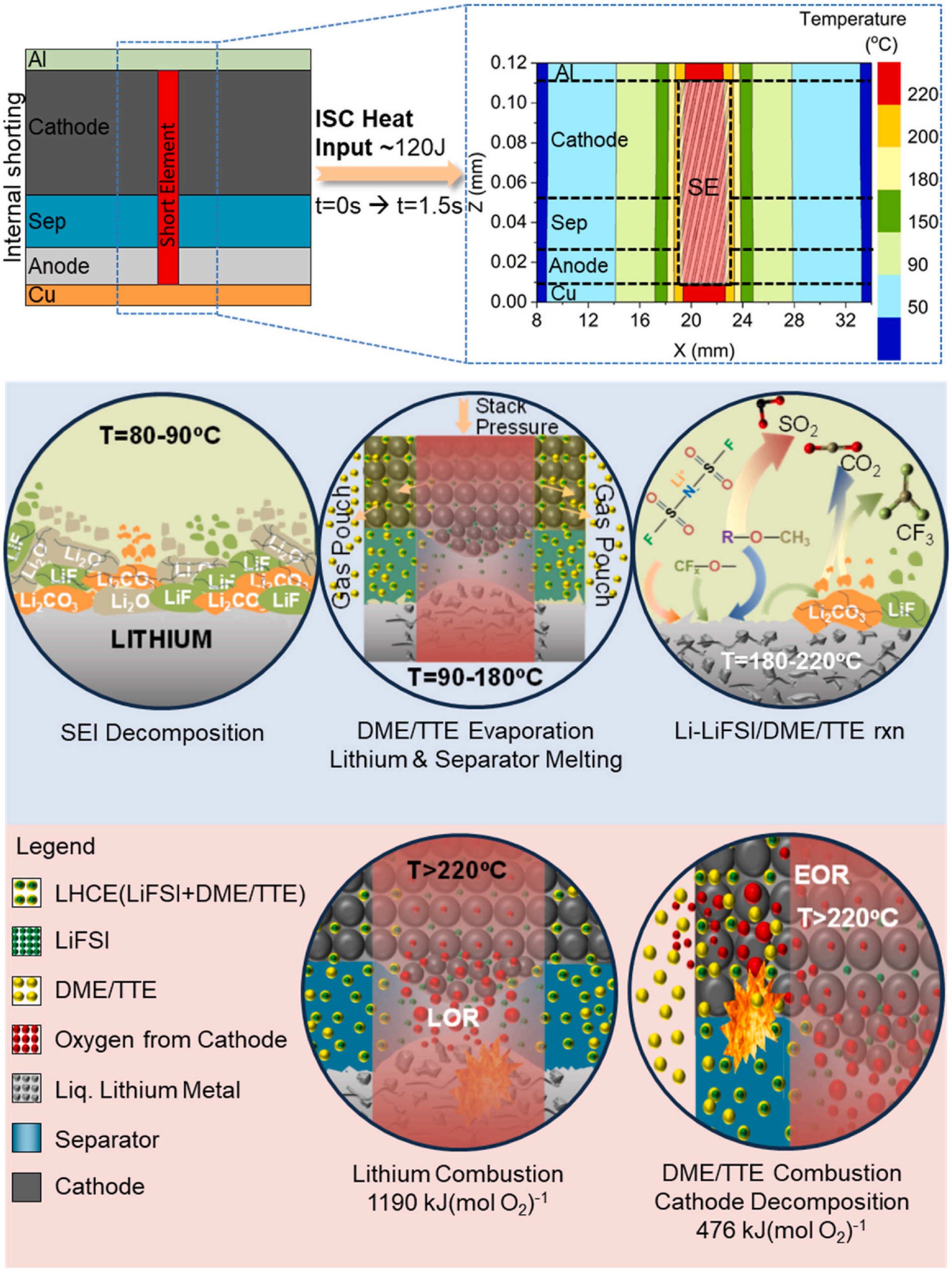

Fig. 5. Internal short-circuit-induced thermal runaway mechanism for AFBs.

heat. The heating power and total heating energy from ISC Joule heat are significantly lower than those from TR reaction heats; therefore, ISC heat only serves as an instigator for TR reactions to start. The TR reaction heats increase the rate of temperature rise in the cell, and the local hot spots become more severe as the difference between the maximum and average anode temperatures increases (Fig. S7). Over time, the heat from the hot spot diffuses, and more cathode area begins releasing oxygen, generating more TR reaction heat and triggering a chain reaction for uncontrolled heat generation. At ~3.1s, the heating power from LOR shoots up, indicating a sudden TR propagation. At ~3.3s, the heating power from TR reactions reaches a maximum, and 80% of oxygen has already been released from the cathode. The increase in both the maximum and average temperatures of the cell above 220 °C indicates that oxygen evolution occurs across the entire cathode footprint. After this, the oxygen release rate subsides, and hence the reaction heating power also reduces. The total oxygen consumed from EOR is 63% of the oxygen released, and from LOR is 8% oxygen released. The remaining oxygen remains dissolved in the liquid electrolyte throughout the cell. The total TR heat energy from EOR is 78%, and from LOR is 22%. This shows the severe nature of the LOR reaction. For the same amount of oxygen consumed, LOR generates 2.5 times more heat compared to EOR.

3.2. Thermal runaway mechanism

Contour plots can provide much better insights into what's happening in each solid layer of the cell. Fig. 4 shows O_2 release contours, O_2 consumption rate by EOR contours, O_2 consumption rate by LOR contours, and temperature contours at different times near the TR propagation time. Fig. S8 shows the cell cross-section where these contour plots are plotted. These contours do not show any instantaneous release of O_2, but the temperature contours reveal a gradual increase till 300 °C, followed by a sudden jump in O_2 release and temperature. This is evident in Fig. 3, which displays volume-integrated results. At 3.2 s, 70% of the cell area exceeds 300 °C, and 100% exceeds 220 °C, indicating the initiation of oxygen release throughout the entire cell. Consequently, this point is the point of TR propagation. The O_2 release contours depict an O_2 release front traveling through the cell. This can be understood as a moving flame front: the maximum temperature increase occurs where O_2 and fuel meet. This reaction releases additional heat, thereby enhancing heat diffusion. The heat that diffuses forward raises the temperature, advancing the O_2 release front. Behind this O_2 release front, the O_2 consumption front by EOR and LOR can be observed. Beyond the consumption front lies the temperature zone exceeding 600 °C, which results from the accumulation of reaction heat diffusion in the opposite direction of the release front.

Based on our study of AFBs, we propose a thermal runaway mechanism (Fig. 5). The heat input from ISC is the instigator of TR. Within 1.5 s, the unshorted layers supply approximately 120 J (J/cm^2, 10x10 short area) of heat to the shorted layer, raising its temperature above 220 °C. The top layer of the figure displays the temperature contours at the time of thermal incident initiation. It shows the layer of the cell at different temperatures ranging from 50 to 220 °C. This temperature range reveals various reactions occurring within the cell in different layers and in varying temperature zones. The second layer of the figure shows the benign reactions, which generate little heat. The first TR reaction starts with SEI decomposition at 80-90 °C. This reaction, although it produces high heat per unit mass, does not contribute significantly to the TR reaction heat (refer to Table 1) during an ISC and is therefore shown in the blue zone in the figure. The other reactions that occur in the range of 90-180 °C are electrolyte evaporation (DME, TTE), separator melting, and lithium melting; the endothermic heat from these reactions is also very low. The reaction between Li and LiFSI, shown in Table 1, releases SO_2 and NO_2 and forms LiF. Also, they react with solvent vapors, evolving CO_2 and forming Li_2CO_3. The heat evolved from this reaction is controversial, but as confirmed by RISC, it does not affect the results of ISC-induced TR. The third layer of the mechanism starts with the cathode decomposition and oxygen evolution. This released oxygen diffuses and migrates to the molten lithium on the anode side, where it reacts with it to form Li_2O and releases $4.3 \times 10^7\ \mathrm{J\,kg^{-1}}$ *(reaction enthalpy,* 0.25 mol *of* O_2 *consumed for* 1 mol *of Li)* of heat. Additionally, the oxygen reacts with solvent vapors, releasing $1.13 \times 10^7\ \mathrm{J\,kg^{-1}}$ *(reaction enthalpy,* 4.07 mol *of* O_2 *consumed for* 1 mol *of electrolyte)* of heat. These two reactions are depicted in the red layer because they are the most heat-generating and can contribute to energetic events such as explosions, cell ruptures, and uncontrolled fires under certain conditions.

4. Conclusion

This study presents an electrochemical-thermal-coupled model to elucidate ISC-induced TR in anode-free lithium batteries. By integrating a validated resistance-controlled internal short circuit (RISC) experimental methodology with high-fidelity numerical modeling, the work successfully isolates single-layer ISC behavior while preserving the electrochemical characteristics of a multilayer cell. The results demonstrate that ISC-generated Joule heating is the primary trigger for TR, rapidly elevating local temperatures to levels that initiate cathode decomposition and oxygen release. Subsequent lithium oxidation and electrolyte oxidation reactions dominate the reaction energetics and govern TR propagation and severity.

The proposed theory-based reaction framework, coupled with oxygen diffusion and consumption kinetics, overcomes key limitations of conventional DSC-based approaches by avoiding reaction overlap and overestimation of heat release. Model predictions show good agreement with experimental measurements of temperature evolution, shorting resistance, current response, and TR onset time. Importantly, the validated simulation model provides a robust platform to systematically investigate TR mitigation strategies. In future studies, this model will be used to simulate reduced state-of-charge conditions, comparisons between power and energy cells, the incorporation of oxygen scavengers or oxygen-blocking layers, and variations in cell design parameters, all of which will be verified with RISC experimental data. Together, this combined experimental-modeling approach offers a predictive tool for safety-conscious design, mitigation assessment, and risk reduction in next-generation high-energy battery systems.

CRediT authorship contribution statement

Nitesh Gupta: Conceptualization, Data curation, Formal analysis, Investigation, Methodology, Validation, Writing – original draft. **Kaiqiang Qin:** Conceptualization, Data curation, Methodology, Resources. **Tatsuro Sasaki:** Supervision, Writing – review & editing. **Koichiro Aotani:** Project administration, Supervision. **Chao-Yang Wang:** Funding acquisition, Project administration, Supervision, Writing – review & editing.

Declaration of competing interest

The authors declare that they have no known competing financial interests or personal relationships that could have appeared to influence the work reported in this paper.

Acknowledgements

Partial support from Nissan Motor Co. Ltd. and Diefenderfer endowment is gratefully acknowledged. Software access and support from Gamma Technologies for GT-Autolion is greatly acknowledged.

Appendix A. Supplementary data

Supplementary data related to this article can be found online at https://doi.org/10.1016/j.jpowsour.2026.240825.

Data availability

Data will be made available on request.

References

[1] B. Liu, J.G. Zhang, W. Xu, Advancing Lithium metal batteries, Joule 2 (5) (2018) 833–845, https://doi.org/10.1016/j.joule.2018.03.008.

[2] X. Shen, H. Liu, X.B. Cheng, C. Yan, J.Q. Huang, Beyond lithium ion batteries: higher energy density battery systems based on lithium metal anodes, Energy Storage Mater. 12 (2018) 161–175, https://doi.org/10.1016/j.ensm.2017.12.002.

[3] S. Nanda, A. Gupta, A. Manthiram, Anode-Free full cells: a pathway to high-energy density lithium-metal batteries, Adv. Energy Mater. 11 (2) (2021) 2000804, https://doi.org/10.1002/aenm.202000804.

[4] R. McGinnis, CO2-to-Fuels renewable gasoline and jet fuel can soon be price competitive with fossil fuels, Joule 4 (3) (2020) 509–511, https://doi.org/10.1016/j.joule.2020.01.002.

[5] Y. Wu, et al., An empirical model for the design of batteries with high energy density, ACS Energy Lett. 5 (3) (2020) 807–816, https://doi.org/10.1021/acsenergylett.0c00211.

[6] W. Xu, et al., Lithium metal anodes for rechargeable batteries, Energy Environ. Sci. 7 (2) (2014) 513–537, https://doi.org/10.1039/c3ee40795k.

[7] C.Y. Wang, et al., Fast charging of energy-dense lithium-ion batteries, Nature 611 (7936) (2022) 485–490, https://doi.org/10.1038/s41586-022-05281-0.

[8] R.V. Salvatierra, W. Chen, J.M. Tour, What can be expected from “Anode-Free” lithium metal batteries? Adv. Energy Sustain. Res. 2 (5) (2021) 2000110 https://doi.org/10.1002/aesr.202000110.

[9] L. Wang, et al., Engineering of lithium-metal anodes towards a safe and stable battery, Energy Storage Mater. 14 (2018) 22–48, https://doi.org/10.1016/j.ensm.2018.02.014.

[10] X. Shen, H. Liu, X.B. Cheng, C. Yan, J.Q. Huang, Beyond lithium ion batteries: higher energy density battery systems based on lithium metal anodes, Energy Storage Mater. 12 (2018) 161–175, https://doi.org/10.1016/j.ensm.2017.12.002.

[11] C.Y. Wang, K. Qin, S. Ge, N. Gupta, T. Sasaki, K. Aotani, Metrics for evaluating safe electrolytes in energy-dense lithium batteries, Nat. Energy 10 (2025) 1382–1390, https://doi.org/10.1038/s41560-025-01887-6.

[12] Xiaomi will cooperate with investigation into fatal EV crash, says founder. https://www.reuters.com/world/china/chinas-xiaomi-says-actively-cooperating-with-police-after-fatal-accident-2025-04-01/, 2025.

[13] Airline bans power banks after plane destroyed in horror fire. https://www.the-independent.com/travel/news-and-advice/south-korea-air-busan-fire-power-banks-b2692417, 2025.

[14] Explosive Battery Blaze in South Korea 'Paralyzes' Vital Government Services, 2025. https://www.cnn.com/2025/09/27/asia/south-korea-fire-data-center-daejeon-intl-hnk.

[15] M.S. Whittingham, Lithium batteries and cathode materials, Chem. Rev. 104 (10) (2004) 4271–4302, https://doi.org/10.1021/cr020731c.

[16] K. Liu, Y. Liu, D. Lin, A. Pei, Y. Cui, Materials for lithium-ion battery safety, Sci. Adv. 4 (6) (2018), https://doi.org/10.1126/sciadv.aas982 eaas9820.

[17] S. Zheng, L. Wang, X. Feng, X. He, Probing the heat sources during thermal runaway process by thermal analysis of different battery chemistries, J. Power Sources 378 (2018) 527–536, https://doi.org/10.1016/j.jpowsour.2017.12.050.

[18] B. Lu, et al., Key parameters in determining the reactivity of lithium metal battery, ACS Energy Lett. 8 (7) (2023) 3230–3238, https://doi.org/10.1021/acsenergylett.3c01001.

[19] C. Zhang, S. Santhanagopalan, M.A. Sprague, A.A. Pesaran, Coupled mechanical-electrical-thermal modeling for short-circuit prediction in a lithium-ion cell under mechanical abuse, J. Power Sources 290 (2015) 102–113, https://doi.org/10.1016/j.jpowsour.2015.04.162.

[20] Daniel H. Doughty, Roth E. Peter, A general discussion of Li ion battery safety, Electrochem. Soc. Interface 21 (2) (2012) 37, https://doi.org/10.1149/2.F03122if.

[21] X. Feng, D. Ren, X. He, M. Ouyang, Mitigating thermal runaway of lithium-ion batteries, Joule 4 (4) (2020) 743–770, https://doi.org/10.1016/j.joule.2020.02.010.

[22] R.S. Longchamps, X.G. Yang, C.Y. Wang, Fundamental insights into battery thermal management and safety, ACS Energy Lett. 7 (3) (2022) 1103–1111, https://doi.org/10.1021/acsenergylett.2c00077.

[23] A. Bates, et al., A multi-scale framework for advancing battery safety through early calorimetric analysis of materials and components, Electrochem. Soc. Interface 33 (3) (2024) 69, https://doi.org/10.1149/2.F10243IF.

[24] S. Ge, et al., Quantification of lithium battery fires in internal short circuit, ACS Energy Lett. 9 (2024) 5747–5755, https://doi.org/10.1021/acsenergylett.4c02564.

[25] N. Gupta, S. Ge, T. Sasaki, K. Qin, R.S. Longchamps, K. Aotani, C.Y. Wang, Simulation of single-layer internal short circuit in anode-free batteries, eTransportation 22 (2024 Dec 1) 100380.

[26] I.T. Song, J. Kang, J. Koh, H. Choi, H. Yang, E. Park, J. Lee, W. Cho, Y.M. Lee, S. Lee, N. Kim, Thermal runaway prevention through scalable fabrication of safety reinforced layer in practical Li-ion batteries, Nat. Commun. 15 (1) (2024) 8294, https://doi.org/10.1038/s41467-024-52766-9.

[27] Y. Liu, Y. Mao, H. Wang, Y. Pan, B. Liu, Internal short circuit of lithium metal batteries under mechanical abuse, Int. J. Mech. Sci. 245 (2023) 108130, https://doi.org/10.1016/j.ijmecsci.2023.108130.

[28] B. Mao, H. Chen, Z. Cui, T. Wu, Q. Wang, Failure mechanism of the lithium ion battery during nail penetration, Int. J. Heat Mass Tran. 122 (2018) 1103–1115, https://doi.org/10.1016/j.ijheatmasstransfer.2018.02.036.

[29] D.P. Finegan, et al., Tracking internal temperature and structural dynamics during nail penetration of lithium-ion cells, J. Electrochem. Soc. 164 (13) (2017) A3285, https://doi.org/10.1149/2.1501713jes.

[30] J. Lamb, C.J. Orendorff, Evaluation of mechanical abuse techniques in lithium ion batteries, J. Power Sources 247 (2014) 189–196, https://doi.org/10.1016/j.jpowsour.2013.08.066.

[31] S. Liu, S. Huang, Q. Zhou, K. Snyder, M.K. Long, G. Zhang, In situ measurement of dynamic internal short circuit resistance during nail penetration of lithium-ion cells and its implications on cell robustness and abuse tolerance, J. Electrochem. Soc. 170 (6) (2023) 060515, https://doi.org/10.1149/1945-7111/acd814.

[32] D.P. Finegan, et al., Characterising thermal runaway within lithium-ion cells by inducing and monitoring internal short circuits, Energy Environ. Sci. 10 (6) (2017) 1377–1388, https://doi.org/10.1039/c7ee00385d.

[33] C.F. Lopez, J.A. Jeevarajan, P.P. Mukherjee, Experimental analysis of thermal runaway and propagation in lithium-ion battery modules, J. Electrochem. Soc. 162 (9) (2015) A1905, https://doi.org/10.1149/2.0921509jes.

[34] W. Zhao, G. Luo, C.Y. Wang, Modeling nail penetration process in large-format Li-ion cells, J. Electrochem. Soc. 162 (1) (2014) A207, https://doi.org/10.1149/2.1071501jes.

[35] R. Zhao, J. Liu, J. Gu, Simulation and experimental study on lithium ion battery short circuit, Appl. Energy 173 (2016) 29–39, https://doi.org/10.1016/j.apenergy.2016.04.016.

[36] T.G. Zavalis, M. Behm, G. Lindbergh, Investigation of short-circuit scenarios in a lithium-ion battery cell, J. Electrochem. Soc. 159 (6) (2012) A848, https://doi.org/10.1149/2.096206jes.

[37] K. Qin, S. Ge, N. Gupta, T. Sasaki, C.Y. Wang, High heat-tolerance and safety of lithium metal batteries using a high-concentration phase-change electrolyte, J. Power Sources 630 (2025) 236094, https://doi.org/10.1016/j.jpowsour.2024.236094.

[38] V. Srinivasan, C.Y. Wang, Analysis of electrochemical and thermal behavior of Li-Ion cells, J. Electrochem. Soc. 150 (1) (2003) A98, https://doi.org/10.1149/1.1526512.

[39] W.B. Gu, C.Y. Wang, Thermal-Electrochemical modeling of battery systems", J. Electrochem. Soc. 147 (8) (2000) 2910, https://doi.org/10.1149/1.1393625.

[40] M. Doyle, T.F. Fuller, J. Newman, Modeling of galvanostatic charge and discharge of the Lithium/Polymer/Insertion cell, J. Electrochem. Soc. 140 (6) (1993) 1526, https://doi.org/10.1149/1.2221597.

[41] D. Puthusseri, M. Parmananda, P.P. Mukherjee, V.G. Pol, Probing the thermal safety of Li metal batteries, J. Electrochem. Soc. 167 (12) (Aug. 2020) 120513, https://doi.org/10.1149/1945-7111/ababd2.

[42] M. Parmananda, B. Ryali, P.P. Mukherjee, Thermo-Electrochemical stability analytics of electrode materials, J. Electrochem. Soc. 167 (12) (2020) 120513, https://doi.org/10.1021/acs.jpcc.9b08980.

[43] E. P. Roth et. al. Instability of PVDF Based Polymeric Binder in lithium-ion Cells: Final Report. Sandia Report, SAND99-1164.

[44] J. Hou, et al., Unlocking the self-supported thermal runaway of high-energy lithium-ion batteries, Energy Storage Mater. 39 (2021) 395–402, https://doi.org/10.1016/j.ensm.2021.04.035.

[45] J. Hou, et al., Thermal runaway of Lithium-ion batteries employing LiN(SO2F)2-based concentrated electrolytes, Nat. Commun. 11 (1) (2020) 5100, https://doi.org/10.1038/s41467-020-18868-w.

[46] Z. Guo, Z. Cui, R. Sim, A. Manthiram, Localized high-concentration electrolytes with low-cost diluents compatible with both cobalt-free LiNiO2 cathode and lithium-metal anode, Small 19 (49) (2023) 2305055, https://doi.org/10.1002/smll.202305055.

[47] H. Jia, et al., Is nonflammability of electrolyte overrated in the overall safety performance of lithium ion batteries? A sobering revelation from a completely nonflammable electrolyte, Adv. Energy Mater. 13 (4) (2023) 2203144, https://doi.org/10.1002/aenm.202203144.

[48] G.G. Eshetu, S. Grugeon, G. Gachot, D. Mathiron, M. Armand, S. Laruelle, LiFSI vs. LiPF6 electrolytes in contact with lithiated graphite: comparing thermal stabilities and identification of specific SEI-reinforcing additives, Electrochim. Acta 102 (2013) 133–141, https://doi.org/10.1016/j.electacta.2013.03.171.